# Chapter 3

# X-Ray Diffraction

X-ray diffraction has been a well-established technique in the field of structural investigations for decades, applied not only by physicists. It represents an important tool for chemists and biologists, too, and played a decisive role in the discovery of the structure of the DNA in 1953. Any method that exploits x rays is based upon their discovery in 1895 by W. C. Röntgen by chance while studying the charge transport in gases [91]. This achievement was rewarded the first Nobel prize in the field of physics ever, in 1901. The first diffraction experiment was performed by Max v. Laue in 1912. Fig 3.1 displays the observed diffraction pattern. With this single photograph, Laue solved at once two major problems of his days: It clearly reveals the crystalline nature of solids and proves that x rays behave like waves. This finding was rewarded the Nobel prize in 1914. The following pages summarize the main aspects of the interaction of these "waves" with crystalline material.

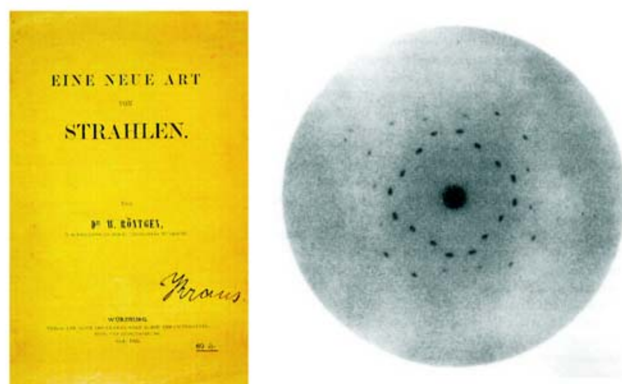


**Figure 3.1:** *Left: Original publication on the discovery of the x rays by W.C. Röntgen [92]. Right: One of the first x-ray diffraction patterns obtained by M.v. Laue in 1912 [93].*

Since x-ray diffraction is a rather old technique, a rich variety of text books exists on this topic. Therefore, not every single result will be documented by a citation in the following. Only those aspects that cannot be found in standard text books are referenced. The interested reader is kindly referred to B. E. Warren [94], J. Als-Nielsen [95] and J.M. Cowley [96].

## 3.1 Basic Quantities

In the classical picture, x rays are electromagnetic waves with wavelengths of the order of Angström (1 Å=$10^{-10}$ m), characterized by their position and time-dependent electric ($\mathbf{E}$) and magnetic ($\mathbf{H}$) fields. In the following we will concentrate on the $\mathbf{E}$-field for the sake of simplicity. The electromagnetic wave can be described by:

$$\mathbf{E} = E_0 \epsilon \, e^{i(\mathbf{kr}-\omega t)} \quad , \tag{3.1}$$

with $E_0$ being the maximum amplitude of the electric field, $\epsilon$ the unit vector pointing along the polarization direction and $\mathbf{k}$ the wave vector towards the propagation direction of the wave with a length given by the wavelength $\lambda$:

$$k = \frac{2\pi}{\lambda} \quad . \tag{3.2}$$

From the quantum-mechanical point of view, such a wave is quantized into photons of energy $\hbar\omega$ and momentum $\hbar k$. The relation between the wavelength $\lambda$ in Å and the photon energy is given by the formula:

$$\lambda[\text{Å}] = \frac{12398}{\hbar\omega \, [eV]} \quad . \tag{3.3}$$

X-ray diffraction originates from the interaction of these photons with the electrons of the material. Most of the basic quantities can be introduced considering the interaction of the electromagnetic wave with the simplest possible unit - only one electron. In the classical picture, the oscillating electric field of the wave forces the electron to vibrate with the same frequency. Hence, the electron is a source of dipole radiation whose frequency equals that of the exciting wave. This radiated wave is described at the point of observation $\mathbf{R}$ ($|\mathbf{R}| = R >> \lambda$) by:

$$E_{rad}(\mathbf{R}, t) = -\frac{e^2}{4\pi\epsilon_0 m_e c^2} \, P_A \, \frac{e^{ikR}}{R} E_{inc}(t) \quad . \tag{3.4}$$

The minus sign accounts for a phase shift of $\pi$ in the scattering process. The energy-independent scattering amplitude of a single electron,

$$r_0 = \frac{e^2}{4\pi\epsilon_0 m_e c^2} = 2.82 \; 10^{-5}\text{Å} \quad , \tag{3.5}$$

known as the Thomson scattering length or the classical electron radius, is the common unit in the description of scattered amplitudes. The coefficient $P_A$ accounts for the angular dependence of dipolar radiation. The wave vector of the scattered wave at the point of observation, $\mathbf{k_{out}}$, and that of the incident wave, $\mathbf{k_{in}}$, span the scattering plane, as sketched in Fig. 3.2. The angle between the two is called the scattering angle $2\Theta$. Since the electron oscillates along $\epsilon$, $P_A$ depends on the direction of the polarization vector $\epsilon$ with respect to the scattering plane:

$$P_A(2\Theta) = \begin{cases} 1 & , \quad \epsilon \perp \quad \text{scattering plane } (\sigma\text{-light}) \\ \cos 2\Theta & , \quad \epsilon \parallel \quad \text{scattering plane } (\pi\text{-light}) \end{cases} \tag{3.6}$$

Scattering from more than one electron causes interference effects. Waves scattered from different points in space travel different paths and consequently exhibit a phase shift at the point of observation (see Fig. 3.2). The total scattered amplitude from an arrangement of scattering centers is given by

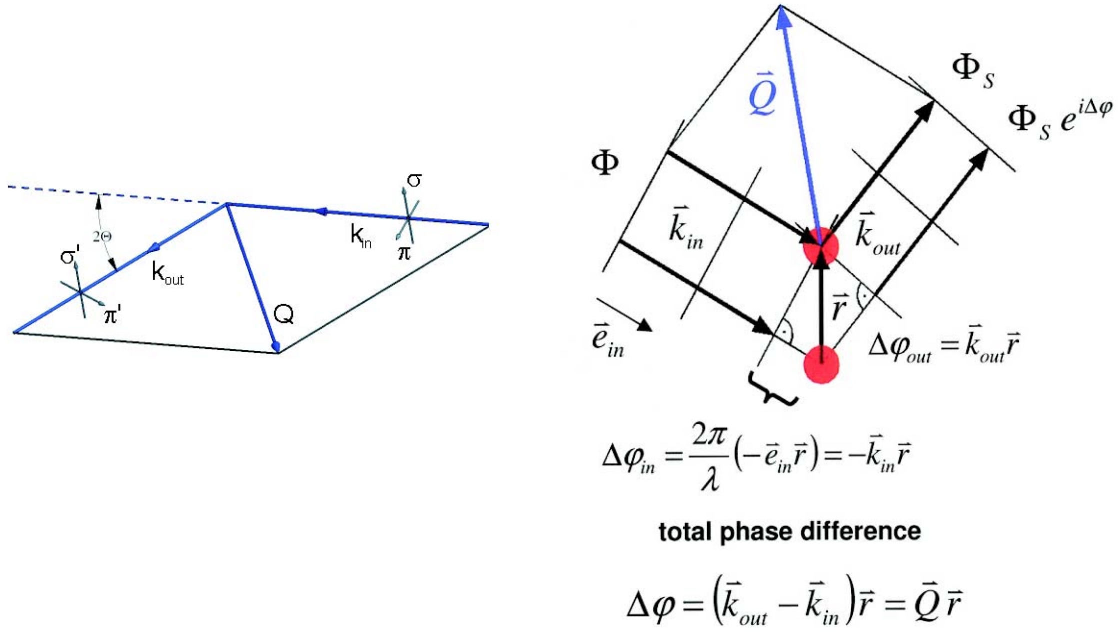


**Figure 3.2:** *Left: The wave vector of the incoming* $\mathbf{k_{in}}$ *and the scattered wave* $\mathbf{k_{out}}$ *span the scattering plane. The angle between the two is called the scattering angle* $2\Theta$*. The momentum transfer in the scattering process is given by the scattering vector* $\mathbf{Q}$*. Right: Phase shift of two waves scattered at two scattering centers of distance* $\mathbf{r}$.

the sum of the individual scattered waves, taking the corresponding phase shifts into account. More general, the amplitude scattered by a continuous charge distribution $\rho(\mathbf{r})$ reads:

$$A(\mathbf{Q}) \propto -r_0 \int_V \rho(\mathbf{r}) e^{i\mathbf{Qr}} d^3r \quad , \tag{3.7}$$

with the phase shift of the wave scattered at $\mathbf{r}$ quantified in terms of the scattering vector $\mathbf{Q}$ (see Fig. 3.2):

$$\Delta\varphi = (\mathbf{k_{out}} - \mathbf{k_{in}})\mathbf{r} = \mathbf{Qr} \tag{3.8}$$

Evaluation of 3.7 for a single atom yields the atomic form factor $f^0(\mathbf{Q})$, which quantifies the scattering strength of the atom as a function of momentum transfer. In the limit $Q \to 0$, all the different volume elements of the atom scatter in phase and the atomic form factor equals the number of electrons in the atom. In general, electrons in an atom cannot be considered as free electrons, but can be treated as forced oscillators. Therefore, the amplitude and phase of their oscillation with respect to the exciting wave will depend on the photon energy. These additional contributions can be taken into account by rewriting the atomic form factor:

$$f(\mathbf{Q}, \hbar\omega) = f^0(\mathbf{Q}) + f'(\hbar\omega) + if''(\hbar\omega) \quad , \tag{3.9}$$

with $f'$ and $f''$ being the dispersion correction to $f^0$. The elastic scattering discussed so far is not the only interaction of photons and matter. Absorption will be an important aspect in this thesis. In this process, the energy of a photon is transferred to an atomic electron, which then is emitted from the

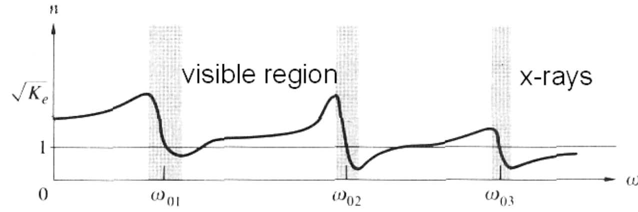


**Figure 3.3:** *Energy dependence of the index of refraction $n$ (from Ref. [97]).*

atom. Consequently, the intensity of a photon beam traversing a material decreases, quantified by the material-dependent absorption coefficient $\mu$:

$$I(z) = I_0 e^{-\mu z} \quad , \tag{3.10}$$

with $I_0$ being the initial intensity outside the material and $I(z)$ the intensity at a distance $z$ from the surface measured along the beam direction. The remaining holes in the atomic shell usually are filled by electrons from outer shells, either by simultaneous emission of a photon or by expelling an additional electron. The first process is called fluorescence, the latter the Auger process. These mechanisms can be exploited for element specific studies, since both, the absorption process and the subsequent emission, are connected to the characteristic atomic energies. The total amount of emitted electrons and/or fluorescence photons can be used to determine $\mu$. It is possible to express $\mu$ in terms of $f''$. Since $f'$ and $f''$ are related by the Kramers-Kronig-relations, absorption studies are a complementary tool to resonant scattering. The quantity that describes the influence of a material on an electromagnetic wave is the index of refraction $n$. In this picture, the wave vector $k$ of a wave in vacuum changes to $nk$ in the medium, which leads to a description according to:

$$e^{inkz} = e^{iRe(n)kz} e^{-Im(n)kz} \tag{3.11}$$

for a wave propagating along $z$. The real part of $n$ specifies the change of the wavelength, which leads to the well-known optical phenomenon of refraction, while the imaginary part describes the attenuation of the wave. Therefore, the interaction of x rays with matter consisting of a large number of atoms can be described either in the refractive picture, where the matter is thought to be a continuum characterized by its index of refraction, or in the atomic scattering picture by evaluating 3.7. The following pages summarize the major aspects of both, since the refraction as well as the scattering picture is used within this thesis.

## 3.2 X-Ray Reflectivity

In the refractive picture, the influence of matter on an electromagnetic wave is described by the material-dependent index of refraction $n$. That property results from the polarizability of the matter, which is mainly due to a displacement of the atomic electrons with respect to the core at high frequencies. Since those electrons are bound, their excitation is usually described in terms of the forced-oscillator model. Therefore, the response of the electrons on an electromagnetic wave depends on the photon energy $\hbar\omega$, i.e. the difference between the frequency of the wave and the resonance frequency of the bound electron. Consequently, $n$ depends on $\omega$. Within the oscillator model, $n$ can

be described by a sum over all contributing resonances [97]:

$$\frac{n^2-1}{n^2+2} \propto \sum_j \frac{f_j}{\omega_{0j}^2 - w^2 + i\gamma_j\omega} \quad , \tag{3.12}$$

where $f_j$ quantifies the weight of the resonance, $\omega_{0j}$ denote the resonance frequencies and $\gamma_j$ the damping due to energy dissipation. As long as the photon energy is smaller than the resonance energy of an electron, the electron will oscillate in phase with the exciting wave and add a positive contribution to the index of refraction, while the oscillation becomes phase shifted by $\pi$ and contributes negative to $n$ at higher photon energies. As a consequence, $n$ is larger than one as long as $\hbar\omega$ is smaller than most of the characteristic atomic energies. This is the case in the optical region, whereas in the x-ray regime $n$ typically becomes less than one (see Fig. 3.3). Like in the resonance catastrophe of the mechanical counterpart, the scattering strength will become strongly enhanced, if $\hbar\omega$ matches a characteristic energy. This gives rise to resonant scattering and is discussed below.

A wave crossing the surface between vacuum and a material experiences a change of its wave vector from $k$ in vacuum to $nk$ in the material, with $n = 1 - \delta + i\beta$ the index of refraction of the material. From the continuity conditions at the interface, all other aspects follow. The first obvious consequence is a phase shift of the electromagnetic wave with respect to the initial wave after passing a medium. This phase shift can be quantified in the case of a plate of thickness $\Delta$ by only a few atomic quantities, thus relating the macroscopic optical parameters $\delta$, $\beta$ to the microscopic atomic properties, as derived in appendix C:

$$g_0 = \frac{2\pi\rho_a r_0 f^0(0)\Delta}{k} \tag{3.13}$$

and

$$n = 1 - \frac{2\pi\rho_a r_0 f^0(0)}{k^2} = 1 - \delta \quad , \tag{3.14}$$

with $g_0$ being the mentioned phase shift, $\rho_a$ the atomic density and $r_0 f^0(0)$ the scattering strength of an atom.

Typical atomic densities are of the order of $\rho_a \approx 0.1\text{Å}^{-3}$. Therefore, $\delta$ is almost negligible in the conventional x-ray range ($\lambda \approx 1\text{Å} \rightarrow \delta \approx 10^{-5}$) and even in the case of soft x rays only a small parameter. This causes refraction effects and reflectivities to be very small and therefore displays a severe limitation in the construction of optical elements for x rays. According to Eq. 3.14, $n$ is less than one. This leads to the phenomenon of total external reflection for angles of incidence smaller than the critical angle:

$$\alpha_c = \sqrt{2\delta} \quad , \tag{3.15}$$

which is of the order of a few degrees for soft x rays and provides the basis of common x-ray optics. Absorption can be included by taking $n$ as a complex quantity:

$$n = 1 - \delta + i\beta \tag{3.16}$$

According to Eq. 3.10 and Eq. 3.11, this directly yields $\beta = \frac{\mu}{2k}$, or in terms of the atomic scattering length $f = f^0(0) + f' + if''$, with $n \equiv 1 - \frac{2\pi\rho_a r_0}{k^2} f$ :

$$f'' = -\beta\left(\frac{k^2}{2\pi\rho_a r_0}\right) = -\left(\frac{k}{4\pi r_0}\right)\sigma_a \quad , \tag{3.17}$$

where $\sigma_a$ denotes the absorption cross section. The fact that the absorption cross section is proportional to the imaginary part of the atomic scattering strength is known as the optical theorem. These relations can be extended to the case of arbitrary angles of incidence by replacing $\Delta$ by $\frac{\Delta}{\sin\Theta}$.

In addition, refraction and reflection has to be taken into account: Electromagnetic waves, passing the interface between two media of different indices of refraction $n_1, n_2$, are partly reflected and partly transmitted. The propagation direction of the transmitted wave will differ from the direction of the initial wave. From the boundary condition at the interface, demanding continuity of the wave and its derivative, Snell's law can be deduced:

$$n_1 \cos\omega_1 = n_2 \cos\omega_2 \quad . \tag{3.18}$$

$\omega_1$ and $\omega_2$ refer to the angles between the propagation directions of the waves and the interface of the media. The same argument yields the Fresnel equations quantifying the amplitude reflectivity $r$ and transmittivity $t$ at small angles in terms of the wave vector transfer $Q_1$ and $Q_2$ in the two media[1]:

$$r(Q_1) = \frac{Q_1 - Q_2}{Q_1 + Q_2} \tag{3.19}$$

$$t(Q_1) = \frac{2Q_1}{Q_1 + Q_2} \quad . \tag{3.20}$$

Equation 3.19 permits to calculate the reflectivity of a homogeneous slab of thickness $\Delta$ as shown in Fig. 3.4. For simplicity, we assume vacuum on both sides of the slab: $n_0 = n_2 = 1$ and $r_{01} = -r_{12} = r$. The calculation has to take multiple reflections into account as shown in Fig. 3.4: The incoming wave is partly reflected at the upper interface and partly transmitted. The transmitted wave is partly transmitted at the lower interface and partly reflected. This reflected wave will be partly reflected, back into the slab, but also partly transmitted at the upper interface. The transmitted part contributes to the total reflected amplitude, but with a phase difference given by $p^2 = e^{iQ_{slab}\Delta}$. Continuation of this process leads to the geometric series:

$$r_{slab} = r - trtp^2 - trrrtp^4 \ldots = \frac{r(1-p^2)}{1-r^2p^2} \quad . \tag{3.21}$$

In the case of multilayers, Eq. 3.21 can be used to calculate the reflectivity by means of the recursive algorithm introduced by Parratt [98]. A typical result is shown in Fig. 3.4 for a 30 nm-thick holmium layer on tungsten at $h\nu = 900$ eV, with the optical parameters $\beta$ and $\delta$ taken from Ref. [99]. Total external reflection occurs at angles of incidence below the critical angle of holmium $\alpha_c(\text{Ho})$. There, the penetration depth of the photons into the material is extremely small. However, a part of this evanescent wave is absorbed in the material and thus the reflected intensity becomes less than one. Above $\alpha_c(\text{Ho})$, the intensity falls off rapidly, modulated by an oscillatory behavior, the so-called Kiessig fringes. The Kiessig fringes result from constructive and destructive interference of x rays reflected from the two interfaces as a consequence of the angular-dependent phase shift. Their period is determined by the thickness of the layer.

At last, we will briefly discuss the influence of a non-perfect interface. For this purpose, it is instructive to simplify Eq. 3.21: In the case of an infinitesimally thin slab $Q\Delta << 1$ and at angles large compared to the critical angle, $r$ will be small and refraction as well as multiple reflections can be neglected. The reflected amplitude, $r_{thin}$, from such a slab of thickness $dz$ reads:

$$r_{thin}(Q) \approx -i\frac{\lambda\rho r_0 dz}{\sin\omega} \quad . \tag{3.22}$$

[1] The given formula applies to $\sigma$-polarized light.

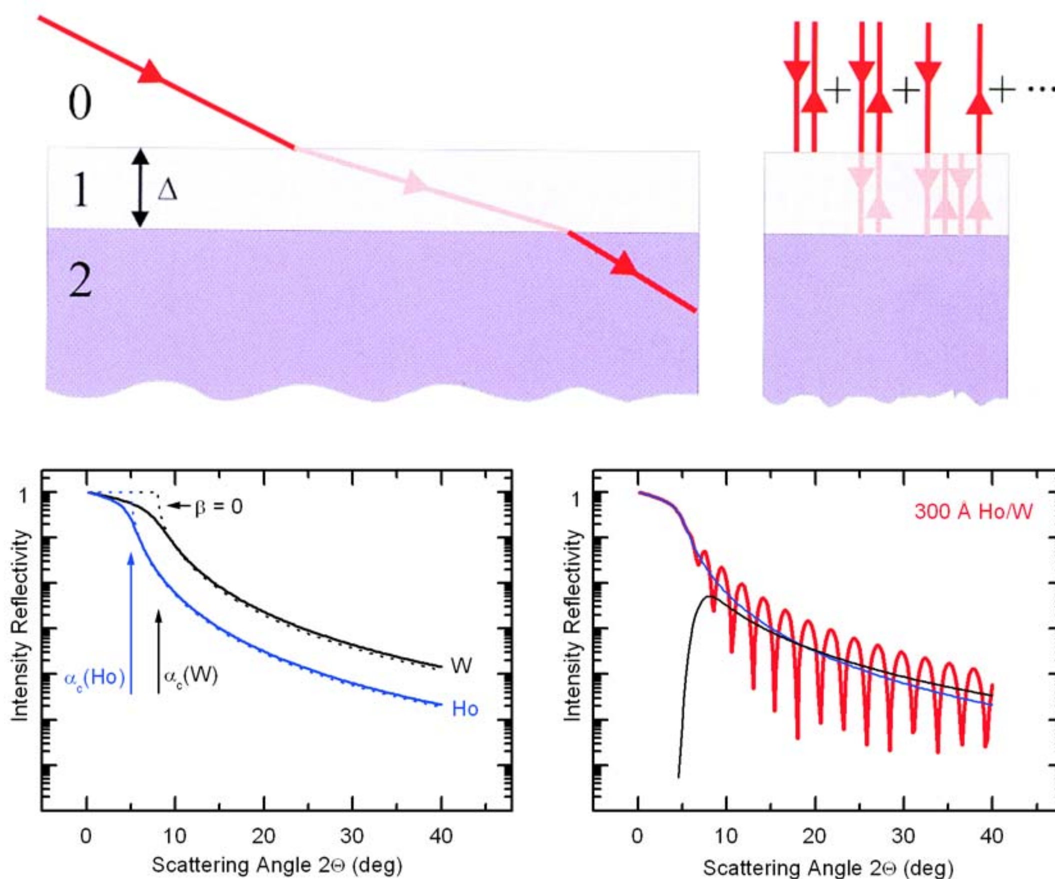


**Figure 3.4:** *Calculated reflectivity of a homogeneous slab. Top, left: Schematic picture, defining the slab of thickness $\Delta$ between two media. Top, right: Multiple reflections (from Ref. [95]. Bottom, left: Calculated intensity reflectivities at $h\nu = 900$ eV of a Ho (blue solid line) and W (black solid line) crystal. The influence of absorption at small angles is shown for comparison: the broken lines correspond to $\beta = 0$. Bottom, right: Calculated intensity reflectivity for a 30 nm-thick holmium film on tungsten (red line). The thinner lines represent the contributions reflected at the Ho surface (blue) and Ho/W interface (black).*

Equation 3.22 now can be applied to the case of a density profile or a rough interface. The reflectivity of a graded interface, with a density profile $f(z)$ along the $z$ direction, is derived from the integral over $f(z)r_{thin}$. The resulting intensity reflectivity can be expressed in terms of the intensity obtained from a perfect interface:

$$\frac{R(Q)}{R_F(Q)} = \left| \int_0^\infty \left( \frac{df}{dz} \right) e^{iQz} dz \right|^2 \quad , \tag{3.23}$$

where $R(Q)$ denotes the intensity reflectivity of the graded interface and $R_F(Q)$ the corresponding Fresnel intensity reflectivity of a perfectly sharp interface. Assuming $f(z) = erf\left(\frac{z}{\sqrt{2}\sigma}\right)$ Eq. 3.23 yields:

$$R(Q) = R_F(Q) e^{-Q^2\sigma^2} \quad . \tag{3.24}$$

More often, a surface or interface deviates from the perfect sharp situation in terms of a roughness, represented by a height profile $h(x, y)$. The integral then becomes a volume integral $dxdydz$ which can be transformed using Gauss' theorem to a surface integral. Assuming a Gaussian statistic of the height fluctuations one finds:

$$\left( \frac{d\sigma}{d\Omega} \right) = \left( \frac{r_0 \rho}{Q_z} \right)^2 \left( \frac{A_0}{\sin \Theta_1} \right) \int e^{-\frac{1}{2} Q_z^2 g(x,y)} e^{i(Q_x x + Q_y y)} dxdy \quad , \tag{3.25}$$

with $g(x, y) =< [h(0, 0) - h(x, y)]^2 >$ describing the ensemble average of height differences. In the case of uncorrelated roughness, i.e. the height differences do not depend on the distance, Eq. 3.25 yields the same result as the graded interface. On the other hand, if the mean height difference is a function of distance (correlated roughness), the reflectivity is no longer confined to the specular direction, but has a diffuse contribution:

$$\left( \frac{d\sigma}{d\Omega} \right) = \left( \frac{d\sigma}{d\Omega} \right)_{Fresnel} e^{-Q_z^2 \sigma^2} + \left( \frac{d\sigma}{d\Omega} \right)_{diffuse} \quad . \tag{3.26}$$

To summarize the information that can be determined from measurements of the specular x-ray reflectivity of a sample: Firstly, known optical parameters $\delta$ and $\beta$ permit to quantify the thickness of a film by means of the Kiessig fringe period. The damping behavior at larger $Q$ determines the mean surface roughness. On the other hand, known sample properties enable to identify the optical parameters.

It should be noted that the reflectivity depends only on the interface properties, but not on the crystallinity of the medium itself, i.e. an unordered layer characterized by well sharp boundaries yields essentially the same reflectivity as a single-crystalline film. If one is interested in these crystalline properties, one has to study structural reflexes. That will be the topic of the following section.

## 3.3 Kinematical Diffraction from a Crystal

In crystalline material, the electron density $\rho$ is characterized by a certain symmetry. Therefore, the evaluation of integral Eq. 3.7 can be split into three parts: The integration over the electron density of only one atom yields the atomic form factor $f^0$ discussed above. Secondly, subsequent accumulation of the contributions originating from the atoms of one unit cell gives the so-called unit-cell structure factor $S_{uc}(\mathbf{Q})$. Finally, the sum over all illuminated unit cells is performed. Hence, the total scattered amplitude of a crystal can be written as:

$$A(\mathbf{Q}) \propto S_{uc}(\mathbf{Q}) \sum_{\mathbf{T}} e^{i\mathbf{QT}} \quad , \tag{3.27}$$

with $\mathbf{T}$ being the set of lattice vectors pointing to illuminated unit cells and

$$S_{uc}(\mathbf{Q}) = -r_0 \sum_{\mathbf{r_i} \in u.c.} f^0_{atom} e^{i\mathbf{Q}\mathbf{r_i}} \tag{3.28}$$

the unit-cell structure factor. The latter term of Eq. 3.27 will be labeled as the lattice sum in the following. In the case of an infinite crystal, Eq. 3.27 leads to infinitely narrow diffraction peaks at reciprocal space positions specified by the condition $\mathbf{QT} = 2n\pi$ for all $\mathbf{T}$, with $n$ an integer number. This can only be fulfilled if $\mathbf{Q} = \mathbf{G}$, with $\mathbf{G}$ is a reciprocal lattice vector. This result corresponds to Bragg's law for diffraction from a set of lattice planes of distance $d$:

$$2d \sin \Theta = n\lambda \quad . \tag{3.29}$$

The intensity of these Bragg peaks is modulated by the unit-cell structure factor $S_{uc}(\mathbf{Q})$. Thus, by measuring the position and relative intensity of the diffraction maxima, one gains information on the lattice and basis that underlies the sample structure. This requires the measurement of several Bragg peaks.

In resonant soft x-ray diffraction, the rather large wavelengths strongly limit the number of accessible Bragg peaks. Consequently, the aim of resonant soft x-ray scattering is only to less extent structure analysis, at least in the conventional sense. Despite the element specificity of resonant scattering, its major advantage is found in its extreme sensitivity to various ordering phenomena that lead to large scattering signals, even from samples of only a few monolayers of material. Therefore, resonant soft x-ray scattering is often applied to systems with at least one strongly limited dimension. For this reason, we will evaluate Eq. 3.27 for the case of a limited number of contributing unit cells. For simplicity, the discussion is limited to cubic symmetry. The lattice sum in Eq. 3.27 then reads:

$$\sum_{\mathbf{T}} e^{i\mathbf{QT}} = \sum_{j_1=1}^{N_1} \sum_{j_2=1}^{N_2} \sum_{j_3=1}^{N_3} e^{i(Q_1 a j_1 + Q_2 a j_2 + Q_3 a j_3)} \tag{3.30}$$

with $Q_i, i = 1, 2, 3$ being the components of the momentum transfer with respect to the lattice, $a$ the lattice constant and $N_i, i = 1, 2, 3$ the number of illuminated unit cells along the corresponding directions. This product of three geometric series can be solved analytically [100]:

$$\left| \sum_{j=1}^{N} e^{i(Qaj)} \right|^2 = \frac{\sin(\frac{N}{2}Qa)^2}{\sin(\frac{1}{2}Qa)^2} \tag{3.31}$$

and yields a scattered intensity of:

$$I(\mathbf{Q}) \propto \prod_{n=1}^{3} \frac{\sin(\frac{N_n}{2}Q_n a_n)^2}{\sin(\frac{1}{2}Q_n a_n)^2} \quad . \tag{3.32}$$

The Laue function (Eq. 3.31) describes a so-called Laue pattern [101] as plotted in Fig. 3.5, characterized by a principal maximum of intensity $N^2$ at the position given by Bragg's law and several side minima of distance $\Delta Q = \frac{2 \cdot \pi}{Na}$. Therefore, the position of the main reflection determines the lattice constant, while the so-called Laue oscillations on both sides quantify the number of contributing layers. In the case of a thin film, only the dimension normal to the surface is limited while the remaining two in-plane dimensions can be treated to be infinite. This causes a rather broad intensity distribution

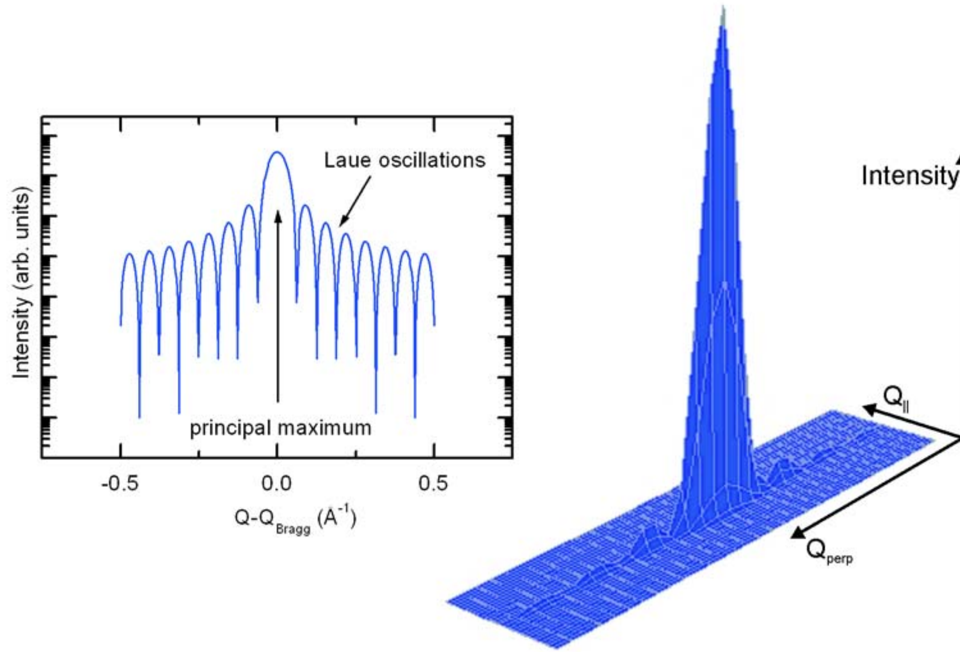


**Figure 3.5:** *Calculated Laue patterns. Left: One-dimensional Laue pattern of a 20-ML film with a layer spacing of 5 Å . Right: Two-dimensional diffraction feature arising from a structure which is strongly limited along the perpendicular direction but large in the parallel direction.*

in reciprocal space along the direction perpendicular to the sample surface, but with a narrow profile describing the $Q_{||}$ dependence (see Fig. 3.5). The scattered intensity then reads:

$$I(\mathbf{Q}) \propto |S_{2D}(\mathbf{Q}_{||})|^2 \left| \sum_{j=1}^{N} e^{i(Q_\perp cj)} \right|^2 \tag{3.33}$$

where $|S_{2D}(\mathbf{Q})|^2$ denotes to the in-plane sum and $N$ the number of layers of distance $c$ perpendicular to the surface.

At this point, the relation between the Laue oscillations and the Kiessig fringes shall be briefly discussed. Both, the distance of two Kiessig fringes as well as that of two Laue oscillations is a measure of the sample thickness: $\Delta Q = \left(\frac{2\pi}{\Delta}\right)_{Kiessig} = \left(\frac{2\pi}{Na}\right)_{Laue}$. However, there is an important difference: The Laue oscillations emerge from the crystalline structure, while the Kiessig fringes originate from the presence of two interfaces, independent of the crystallinity of the material in between. Consequently, the Kiessig fringes are extremely sensitive on the qualities of the interface while the Laue oscillations depend only weakly on properties like surface roughness but are sensitive to crystalline disorder. Therefore, the two provide complementary information: the Kiessig fringes determine the total thickness of a sample, while the Laue oscillations probe the size of the crystalline ordered volume.

In the kinematical description of diffraction, the scattered intensity approaches infinity in the limit $N \longmapsto \infty$. This is of course an absurd result since the scattered intensity can never exceed the intensity of the incident beam for energy conservation. Therefore, this kinematical result can be valid only in the limit of weak interactions and small crystals. To overcome this limitation a dynamical theory of scattering was developed, which will be the subject of the next chapter.

## 3.4 Dynamical Theory

The previous chapter has shown that in the case of a large crystal the results of the kinematical scattering theory can violate the law of energy conservation. Hence, the analysis of experimental data always has to question whether or not the kinematical picture applies. In x-ray diffraction, this is typically the case, even in scattering from hundreds of layers. However, the maximum size of a system that can be described within the kinematical approximation depends on the atomic scattering strength, or more precisely, on the reflectivity per layer. In the present thesis, the huge enhancement of the scattering cross sections at lanthanide-$M_5$ absorption thresholds is exploited. Therefore, the validity of the kinematical theory might be much stronger limited than in off-resonant scattering.

The reason for that breakdown of the kinematical picture can be identified by its obvious oversimplification: The kinematical theory disregards the interaction of the incident primary beam with the scattered waves as well as other aspects of the influence of the material on the photon beam. In the kinematical description the primary beam is the same at all layers, no matter how far from the surface, except for a phase shift due to path differences. This simple picture does not include various aspects: First, each time the primary beam passes a layer, it experiences an additional phase shift $g_0$ as derived in Eq. 3.13. This phase shift leads to a deviation of the position of the maximum of scattered intensity from that specified by Bragg's law. Secondly, absorption of photons will reduce the amplitude of the primary beam with increasing depth. Consequently, the relative contribution of an individual layer to the total scattered amplitude will decrease with increasing distance of the layer from the surface. Both aspects can be included into the kinematical calculation by taking the scattering vector as a complex quantity.

However, the key to ensure energy conservation can be found in a proper incorporation of the interaction of the primary beam and the scattered waves which becomes evident from the inspection of Fig. 3.6(a): Each time the primary beam traverses a layer, a certain portion of photons is reflected. Close to the Bragg angle, all the waves reflected from the different layers are in phase, which leads to the expected maximum of reflection. But, in this case also the reflected waves make the correct Bragg angle with the layers. Each time such a reflected wave passes a layer on its way towards the surface a certain portion is reflected back into the direction of the primary beam. All these secondary reflected waves now also interfere constructively. Since secondary reflected and primary beam are almost completely out of phase, their interference can significantly weaken the total beam intensity along the direction of the incident beam. This, of course, requires the number of layers to be so large that these very weak secondary reflected waves can sum up considerably. The theory that takes these multiple reflections into account is known as the dynamical theory of diffraction. It was discussed first by Darwin in his fundamental two publications in 1914 [102, 103]. Further improvements are due to Ewald and Laue. In literature several review article [104–106] exist, and the interested reader is kindly referred to those in order to get a complete picture. In the present work only the main mechanism is introduced following essentially the original treatment of C. G. Darwin. In addition, absorption will be neglected for the sake of simplicity.

To start with, consider only a single atomic-layer in an x-ray beam as shown in Fig. 3.6 (b). The wave represented by its amplitude and phase $T$ just above the layer is partly reflected and partly transmitted. The reflected wave $S$ is given by the amplitude reflectivity per layer $g$ and a phase shift of $-\frac{\pi}{2}$: $S = -igT$, where $g$ can be calculated from Eq. 3.22. According to Eq. 7.32 the transmitted wave reads $T = (1 - ig_0)T$. We can extend this discussion to an infinite number of layers (see Fig. 3.6 (c)): As in the case of a single layer, the wave field $T$ describes the waves propagating along the direction of the primary beam and the wave field $S$ represents the waves reflected towards the surface. At each layer a part of the $T$ field is transmitted but another part is reflected and contributes to the $S$

field. The $S$ field is as well partly transmitted and partly reflected and consequently contributes to the $T$ field. Therefore, the $T$ and $S$ wave fields are coupled. To be more quantitative, the $S$ field above the $j^{th}$ layer is composed of that part of the $T$ field above the $j^{th}$ layer, which was reflected and that part of the $S$ field below the $j^{th}$ layer, which was transmitted. Let $S_j$ and $S_{j+1}$ be the $S$ field just above the layer $j$ and $j+1$ and $T_j$ the $T$ field just above the $j^{th}$ layer one gets:

$$S_j = -igT_j + (1 - ig_0)S_{j+1}e^{i\phi} \quad , \tag{3.34}$$

where $e^{i\phi}$ accounts for the path difference between the $j^{th}$ and $(j+1)^{th}$ layer given by $\phi = Qd/2$. In the same way, the $T$ wave field just below the $j^{th}$ layer is made up of the transmitted part of $T_j$ and the part of $S_{j+1}$ reflected from the bottom of the $j^{th}$ layer:

$$(1 - ig_0)T_j = T_{j+1}e^{-i\phi} + igS_{j+1}e^{i\phi} \tag{3.35}$$

A solution fulfilling that set of coupled equations can be found by exploiting 3.35 to eliminate $S_j$ and $S_{j+1}$ from 3.34. With the trial solution $T_j = x^j$ Eq. 3.34 becomes a quadratic conditional equation for $x$. Taking the root for $x$ that ensures energy conservation ($|x| \leq 1$), from Eq. 3.34 and Eq. 3.35 the intensity reflectivity $\left(\frac{S_0}{T_0}\right) \cdot \left(\frac{S_0}{T_0}\right)^*$ can be calculated for an infinite perfect crystal. In the case of a finite crystal of N layers one can solve the equations recursively. A typical result is shown in Fig. 3.6(d) for $g = g_0 = 10^{-3}$ for the case of an infinite crystal and a film consisting of 3000 layers. The calculated reflectivity can be divided into two regions: far away from the principal maximum the reflectivity is rather small. The phases of the waves reflected from the individual layers strongly vary. Therefore, the scattered amplitudes do not add constructively and the total reflected intensity is small. The same holds for the secondary scattered beam and consequently the superposition of the primary beam and the secondary scattered waves deviates only weakly from the primary wave itself. This is the region, where the kinematical theory is still valid even for large crystals. The situation changes completely in the vicinity of the Bragg peak. In this case, all the scattered waves in the direction of the S field add constructively as well as all the secondary reflected waves in the direction of the primary beam. Since each secondary reflected wave experienced two times a phase shift of $-\frac{\pi}{2}$ this beam of secondary reflected waves is almost out of phase with the primary beam and causes a rather fast decrease of the wave field in the direction of the primary beam. This is the region, where dynamical theory has to be applied. As can be seen in Fig. 3.6(d), the dynamical reflectivity curve shows a quite different shape compared to the kinematical Laue pattern. It is characterized by a region of total reflection in the vicinity of the Bragg peak, but the reflected intensity never exceeds 100%. That peak is symmetric as long as one neglects absorption effects. Including absorption, the dynamical peak becomes less intense and asymmetric.

To summarize, the reaction of the scattered waves on the primary beam ensures the energy conservation in the case of a strong reflectivity per layer or a large number of layers. The attenuation of the primary beam is then rather dominated by extinction than absorption effects. As a rule of thumb, the kinetic treatment is applicable as long as the reflectivity per layer times the number of layers is smaller than one $Ng << 1$. This thesis deals with resonant diffraction studies, characterized by amplitude reflectivities per layer $g$ as large as $5 \cdot 10^{-3}$. However, the typical sample thicknesses below 50 ML suggest that a full dynamical treatment is not necessary. This finding is further supported by the fact that the huge amplitude reflectivities in the present experiments are always accompanied by a strong photon absorption [107]. Therefore, even in thicker samples the attenuation of the primary beam is dominated rather by photon absorption than by extinction effects. Thus, in the data analysis of this work a modified kinematical description can be applied that takes the strong absorption and non-negligible refraction in form of a complex scattering vector into account.

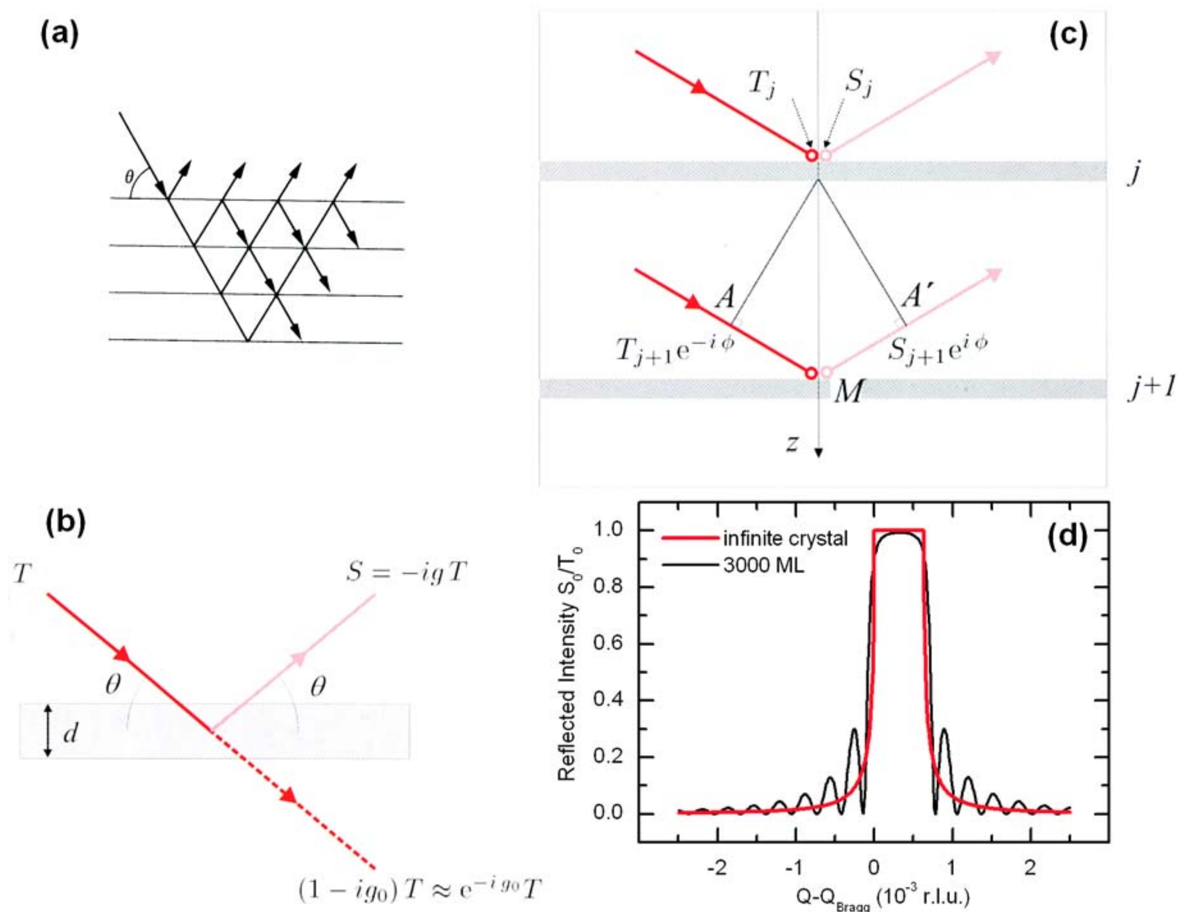


**Figure 3.6:** *(a) Multiple reflections of a wave of an angle of incidence that equals the Bragg condition of constructive interference for a set of lattice planes. (from Ref. [94]). (b) Influence of a single layer on an incident wave $T$, which is partly reflected and partly transmitted. The reflected wave is labeled $S$. $g$ and $g_0$ are small parameters described in the text, from Ref. [95]. (c) Extension to an infinite number of layers. (from Ref. [95]). (d) Calculated reflectivity curves for an infinite crystal (red) and a system consisting of 3000 layers (black). $Q_{Bragg}$ represents the peak position calculated according to Bragg's law.*

## 3.5 Resonant Magnetic Soft X-Ray Scattering

The previous chapter introduced the main concepts of x-ray scattering from crystalline matter. So far, only the interaction between the charge of the electrons and the electric field of the photon was considered. But there is also an interaction with the spin moment of the electrons that causes a magnetic scattering contribution [108, 109]. This magnetic scattering amplitude $f^{mag}$ has the form [110, 111]:

$$f^{mag} = i\, r_0 \, \frac{\hbar\omega}{mc^2} \left[ \frac{1}{2} \mathbf{A}\, \mathbf{L}(\mathbf{Q}) + \mathbf{B}\, \mathbf{S}(\mathbf{Q}) \right] \quad , \tag{3.36}$$

where $\mathbf{L}$ and $\mathbf{S}$ denote the Fourier transforms of the atomic orbital and spin moment densities, respectively, and $\mathbf{A}$ and $\mathbf{B}$ describe the polarization dependences. The structure of Eq. 3.36 is very similar to the magnetic neutron scattering strength. However, in magnetic x-ray scattering $\mathbf{A}$ and $\mathbf{B}$ are not identical, which permits a direct experimental separation of spin and orbital scattering contributions. As a consequence of the factor $\frac{\hbar\omega}{mc^2}$, however, the associated scattering strength is very weak. The magnetically scattered intensity from a sample is further reduced, since only unpaired electrons contribute to the magnetic scattering signal. Hence, the non-resonant magnetic scattering signal is about 6 orders of magnitude smaller than the charge scattering intensity. For this reason, it took more than half a century after the first charge scattering experiment by M. v. Laue until the first magnetic scattering experiment was performed by Bergevin and Brunel on AFM NiO [112]. It is not surprising that this first magnetic x-ray scattering study was performed on a simple antiferromagnet since this structure ensures an optimum separation of charge and magnetic scattering contributions in reciprocal space, an advantage which will be also exploited in the studies of EuTe presented later. Hence, magnetic neutron scattering is the unrivaled method of choice for the determination of magnetic structures.

But there is a way to overcome the limitation of small intensities in x-ray scattering from magnetic materials, namely resonant magnetic x-ray scattering. In resonant scattering, there is an additional contribution to the scattering amplitude caused by the excitation of a core-level electron into an unoccupied intermediate state and the subsequent decay with emission of a photon. The cross section for the whole elastic scattering process is given by [113]:

$$w = \frac{2\pi}{\hbar} \left| \langle f|H_{int}|i\rangle + \sum_n \frac{\langle f|H_{int}|n\rangle \; \langle n|H_{int}|i\rangle}{E_i - E_n + \hbar\omega + i\Gamma/2} \right|^2 \quad , \tag{3.37}$$

where the Hamiltonian $H_{int}$ describes the interaction of the electromagnetic wave with the bound electrons. The first term represents the non-resonant Thomson scattering, while the latter, involving the excitation of an initial state $|i\rangle$ into an intermediate state $|n\rangle$, quantifies the additional resonant contribution. This contribution can become very large for photon energies $\hbar\omega$ that equal the resonance energy $E_i - E_n$. The particular potential of resonant scattering, however, results from a high sensitivity to the intermediate state $|n\rangle$. While in the non-resonant process the change of the valence of an atom by one usually causes only a very small difference in the scattered amplitude, the resonant scattered signal strongly depends on even small changes of the degree of occupancy of the intermediate state. Hence, the resonant scattering process is very sensitive to charge and orbital ordering phenomena as present in the transition metal oxides. A comparable mechanism, illustrated in Fig. 3.7, causes the magnetic sensitivity: The absorption probabilities of left and right circularly polarized photons (LCP, RCP) are different due to the dipole selection rules applied to the already fully occupied $|1, -1\rangle$ state. This leads to an asymmetry in the absorption of photons of different helicities, depending on the direction of the local magnetization, known as the x-ray magnetic circular dichroism (XMCD) in

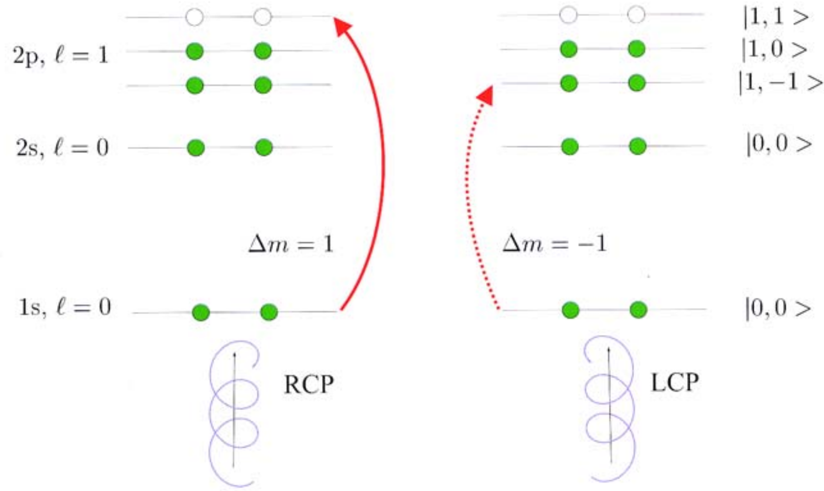


**Figure 3.7:** *Simplified energy level diagram of an atom containing 8 electrons. The dipole selection rule $\Delta m = +1$ for RCP photons and $\Delta m = -1$ for LCP photons causes an asymmetry in the absorption probability of both polarizations since the $\Delta m = -1$ transition is not possible as a consequence of the already fully occupied $|1, -1\rangle$ state (from Ref. [95]).*

absorption. Since the absorption coefficient is related to the imaginary part of the atomic scattering strength by the optical theorem and both, real and imaginary parts of the dispersion correction are related, this asymmetry also manifests in the atomic scattering strength, which consequently depends on the local direction of the magnetization. One of the first studies that exploited the mechanism was performed by Doon Gibbs et al. in 1988 [74] on the spiral antiferromagnet holmium at the Ho $L_3$ absorption threshold. This resonance led to a fifty-fold enhancement of the magnetically scattered intensity. At this photon energy, dipole excitations from the $2p$ into the $5d$ states and quadrupolar excitations into the $4f$ states are involved in the scattering process. Since the $4f$ electrons are responsible for the magnetism of holmium, while the $5d$ states are only indirectly polarized, both resonant scattering contributions are of comparable magnitude. In contrast, at the lanthanide-$M_{4,5}$ absorption thresholds in the soft x-ray range, the dipolar excitation into the $4f$ states is the dominant mechanism. This direct dipole excitation into the states responsible for the magnetism results in a much larger magnetic scattering strength. The resonant scattering amplitude for such a dipole excitation was calculated by Hannon [114], who predicted a magnetic scattering amplitude of the order of $100r_0$ at the lanthanide-$M_{4,5}$ absorption thresholds:

$$f^{res} = (\epsilon_{\mathbf{f}}^* \cdot \epsilon_{\mathbf{i}})F^0 + i(\epsilon_{\mathbf{f}}^* \times \epsilon_{\mathbf{i}})\mathbf{m}F^1 + (\epsilon_{\mathbf{f}}^* \cdot \mathbf{m})(\epsilon_{\mathbf{i}} \cdot \mathbf{m})F^2 \quad . \tag{3.38}$$

Here, the $F^i$ are connected to the energy-dependent dimensionless resonant oscillator strengths for dipole transitions and $\epsilon_{\mathbf{i}}$ and $\epsilon_{\mathbf{f}}$ denote the polarization vectors of the incident and scattered light. Equation 3.38 consists of three parts: The first term describes resonant charge scattering, the latter two depend on the unit vector $m$, pointing along the local magnetization direction. The term linear in $m$ corresponds to the circular dichroism while the latter, of second order in $m$, describes linear dichroic effects. Recent studies quantified these magnetic scattering amplitudes at the Ho- and Gd-$M_{4,5}$ edges to be as large as $240r_0$ [54, 115] as predicted by Hannon. Equation 3.38 reveals that the three resonant scattering contributions have different polarization dependences. The resonant charge scattering shows the same polarization dependence as the non-resonant Thomson scattering. There-

fore, this mechanism does not allow a change of the polarization in the scattering process and exhibits a Brewster angle of vanishing scattered intensity at about 90° of scattering angle for $\pi$-polarized incident light. In contrast, the polarization factor of the circular dichroic $\pi \rightarrow \pi$ channel approaches its maximum at this angular position. In general, the resonant magnetic scattering process involves changes of the polarization and the corresponding polarization factors depend on the direction of $m$, which can be used to determine the magnetization direction.

In addition to the enhancement of the scattering cross section, The resonant x-ray scattering process is characterized by a strong photon absorption in the material. Consequently, the corresponding technique is rather surface sensitive and in particular well suited to study thin films and nanostructures. Furthermore the strong variation of the attenuation length of the photons across the resonance can be utilized for depth-dependent measurements [70]. While the first resonant scattering experiments were performed at several keV of photon energy, the most interesting resonances in the case of magnetic scattering are those, where the intermediate states are responsible for the magnetic properties. For the most prominent magnetic materials these resonances, namely the $L_{2,3}$ edges of the $3d$-transition metals and the $M_{4,5}$ absorption threshold of the lanthanides, are located in the soft x-ray range (100 eV - 1500 eV). This energy region also contains the K-edges of the elements C, N, O, which are the key elements of organic materials. Despite the limitation that mostly chemical and simple ferromagnetic reflections are not accessible as a consequence of the small diameter of the Ewald sphere in the soft x-ray regime, the typical wavelengths in this energy region perfectly match the relevant length scales in antiferromagnets, multilayers, nanostructures and organic molecules, which are of considerable scientific and technological interest.

## 3.6 Typical Scans in Reciprocal Space

The scattering theory discussed above quantifies the scattered intensity as a function of the scattering vector $\mathbf{Q}$. A typical x-ray diffraction experiment, on the other hand, records the intensity in real space as an angular-dependent property. In order to apply the theoretical description to the measured intensity distributions, one has to calculate $\mathbf{Q}$ from the relative orientation and position of the sample surface, the detector and the incident light as well as from the photon energy. These relations are discussed in the following.

The scattering vector $\mathbf{Q}$ is given by the difference of the wave vectors of the incident and reflected light $\mathbf{Q} = \mathbf{k_{out}} - \mathbf{k_{in}}$ (see Fig. 3.8 (a)). In the case of elastic scattering ($|\mathbf{k_{in}}| = |\mathbf{k_{out}}| = k$), its length only depends on the photon wavelength and the scattering angle $2\Theta$:

$$|\mathbf{Q}| = 2k\ \sin\Theta \tag{3.39}$$

At constant photon energy, the accessible reciprocal space is a sphere of radius $2k$ as shown in Fig. 3.9(a). Therefore, the length of the scattering vector $|\mathbf{Q}|$ is exclusively determined by the position, where the scattered light is detected, since the direction of $\mathbf{k_{in}}$ is given by the fix x-ray beam of the photon source. Additional rotational degrees of freedom are needed to change the relative orientation of $\mathbf{Q}$ with respect to the coordinate system of the sample. Figure 3.8 displays the typical situation and defines the angles and axes used in the following. $x$ and $y$ label the axes within the surface plane of the sample and $z$ the normal direction. $Q_x, Q_y$ and $Q_z$ refer to the corresponding reciprocal space directions. $\mathbf{Q}$ is related to four angles: $\mathbf{k_{in}}$ and $\mathbf{k_{out}}$ define the scattering plane and the scattering angle $2\Theta$. $\omega$ ($\widetilde{\Theta}$) denotes the angle between the intersection line of the sample surface with the scattering plane and $\mathbf{k_{in}}$ ($\mathbf{k_{out}}$), whereas $\chi$ describes the tilt between the scattering plane and the surface normal. $\Phi$ quantifies the azimuthal orientation of the sample surface. Thus, four rotational degrees of freedom

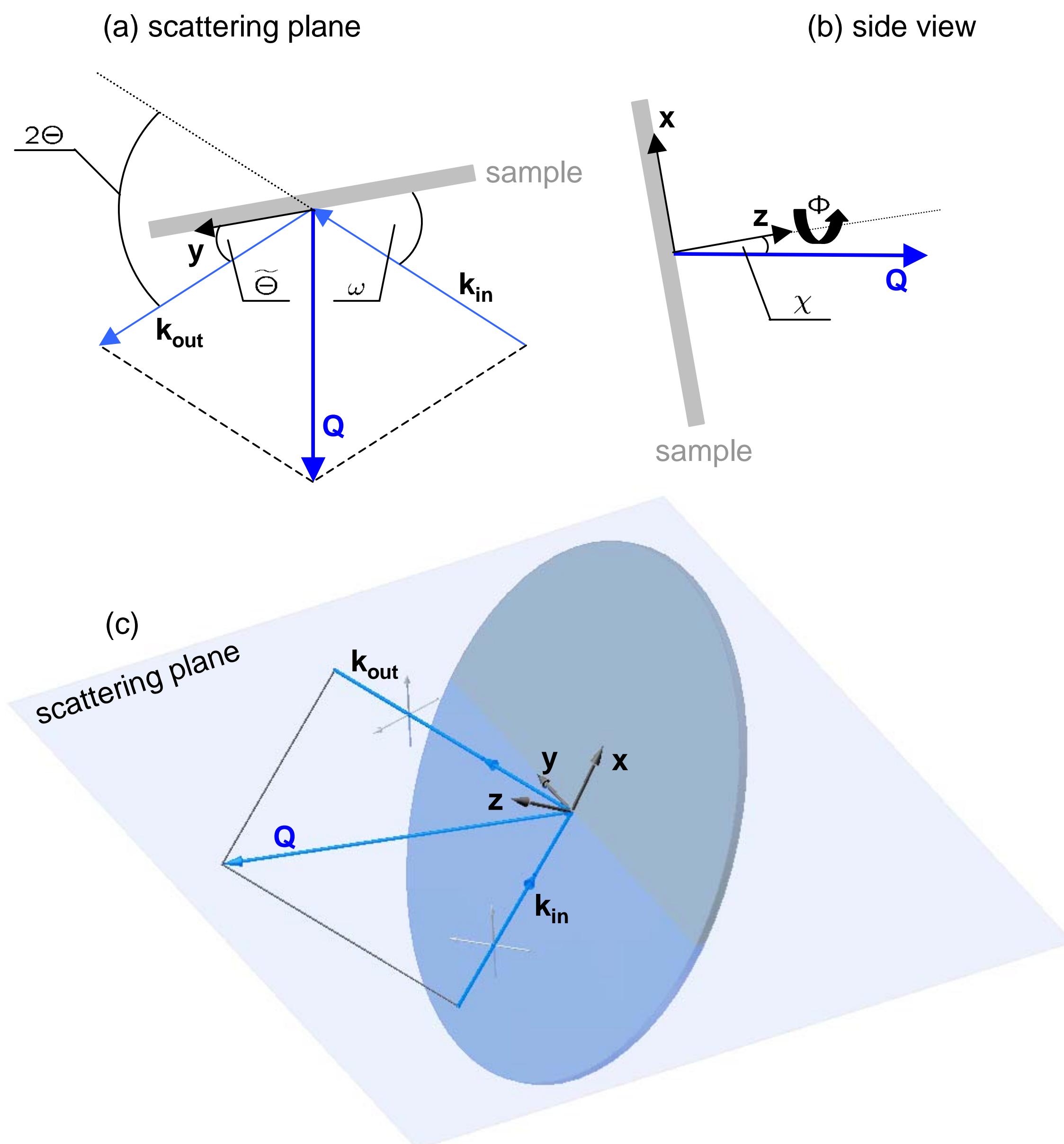


**Figure 3.8:** *The scattering plane and the angles describing the geometry. (a): The scattering plane spanned by the wave vectors of the incoming and scattered light. The scattering angle $2\Theta$ determines the length of the scattering vector* $\mathbf{Q}$. *(b): The angle $\chi$ describes the tilt between the sample surface and the scattering plane. (c): General scattering geometry and the sample coordinate system used throughout this thesis. The shaded blue area represents the scattering plane.*

manipulating $\omega, 2\Theta, \chi$ and $\Phi$ give access to any position in the reciprocal space of the sample within the sphere of radius $2k$.

Diffraction experiments are often restricted to the reflection geometry and therefore to the half space $Q_z \geq 0$. All experiments presented in the last part of this thesis were performed in the so-called horizontal scattering geometry, with horizontally oriented $\mathbf{k_{in}}$ and $\mathbf{k_{out}}$ and the surface normal being within the scattering plane ($\chi = 0$). In case that in this geometry only $\omega$ and $2\Theta$ are varied, the accessible reciprocal space will be a two-dimensional area confined to $|\mathbf{Q}| \leq 2k$, $Q_z \geq 0$ and in addition, restricted to angular positions where neither the detector nor the incoming photon beam is shaded by the sample, which is represented by the blue area in Fig. 3.9(b). This figure further shows the typical paths through reciprocal space that belong to the applied scan modes in the experiments.

The most important scan mode for the present work is a longitudinal or $\Theta/2\Theta$-scan, which exclusively probes the $Q_z$ direction (red line in Fig. 3.9(b)). It is realized by means of a combined rotation of the detector and the sample, such that the angles of incidence and detection are always equal $\omega = \widetilde{\Theta} = \Theta$ (specular geometry). Hence, this scan mode only varies the length of the scattering vector, which in each step points along the surface normal direction. This mode is also used to record the surface reflectivity.

During a transversal or rocking scan, on the other hand, only the sample is rotated ($\widetilde{\Theta} + \omega = 2\Theta =$ const.). Therefore, $\mathbf{Q}$ is of constant length, but describes a circular arc in reciprocal space (black line in Fig. 3.9(b)), which is quantified by:

$$\begin{aligned} Q_z &= Q\ \cos\Delta\omega \\ Q_{||} &= Q\ \sin\Delta\omega \end{aligned}$$

with

$$\begin{aligned} Q &= 2k\ \sin\Theta \\ \omega &= \Theta \pm \Delta\omega \quad . \end{aligned}$$

For small $\Delta\omega$, this path is essentially normal to $Q_z$. Hence, rocking scans can be used to probe the in-plane direction of the sample surface.

A pure rotation of the detector changes both, the length of $\mathbf{Q}$ and the relative magnitudes of its in- and out-of-plane components. A typical path is shown in Fig. 3.9(b) (gray line). Such a scan will be referred to as a detector-scan in the following.

An energy scan, on the other hand, records the scattered intensity as a function of photon energy, providing thereby spectroscopic information, which can be very important in order to clarify the mechanism responsible for a diffraction feature in the case of systems where orbital, charge and magnetic ordering might be simultaneously present, e.g. in the transition metal oxides.

In the following part of this thesis, the technical realization of the required rotational degrees of freedom is discussed. The used scattering apparatus is a two-circle diffractometer, which provides the two most relevant degrees of freedom, namely the $\omega$ and $2\Theta$ rotations. With this diffractometer, any point in the reciprocal space given by the blue area of Fig. 3.9(b) can be reached. In the experiments presented later, the entire blue shaded three-dimensional volume in Fig. 3.9(a) could be accessed by by means of a sample rotation around the surface-normal ($\Phi$) via an in-vacuum screw driver. Very recently a new sample goniometer providing a motorized $\Phi$ manipulation was developed and built in our group [116]. This goniometer will allow for precise $\Phi$-dependent scans in future studies.

The special challenge of building a soft x-ray diffractometer results from the strong absorption of soft x rays in air. That requires to have the detectors and samples within at least a high vacuum

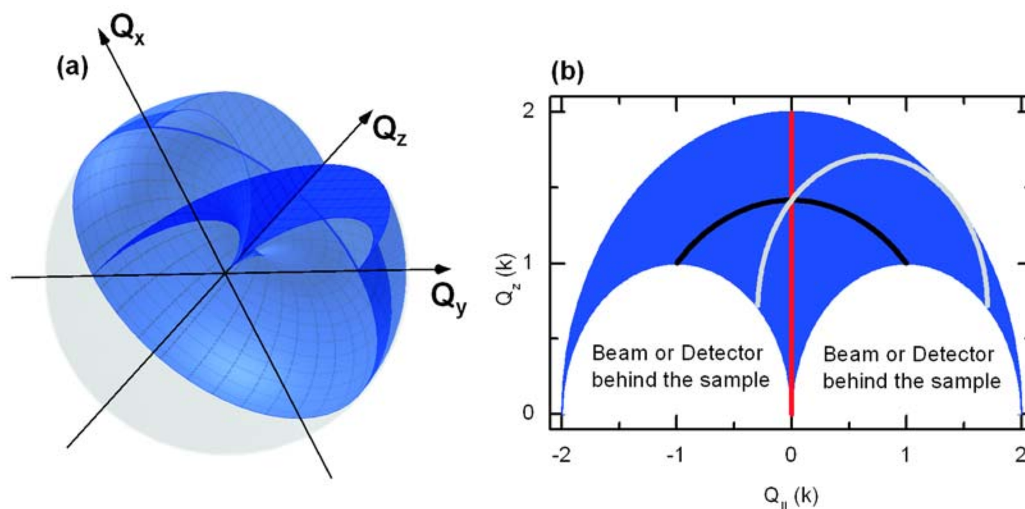


**Figure 3.9:** *Accessible reciprocal space with the built scattering apparatus. (a): The gray sphere of radius $2k$ displays the maximum achievable reciprocal space set by the wavelength of the photons. A two-circle diffractometer in the horizontal reflection geometry is limited by the sample horizon, which restricts the accessible reciprocal space to the blue shaded area. A $\Phi$ rotation extends the accessible positions to the blue volume. (b): Accessible reciprocal space with a two-circle diffractometer in horizontal reflection geometry (blue). The lines represent the paths through this area for the applied scan modes: Longitudinal scan (red), rocking scan at $2\Theta$=90° (black) and detector scan at $\omega$=45° (gray).*

chamber, directly attached to the beamline and particularly prevents the use of a commercialized diffractometer. Within the framework of this thesis a new scattering apparatus was designed and built. Its description and characterization will be the subject of the following chapter.